

## Q-compensated viscoelastic reverse time migration using mode-dependent adaptive stabilization scheme

Yufeng Wang<sup>1</sup>, Hui Zhou<sup>1</sup>, Xuebin Zhao<sup>1</sup>, Qingchen Zhang<sup>2</sup>, and Yangkang Chen<sup>3</sup>

### ABSTRACT

The  $Q$ -compensated viscoelastic reverse time migration ( $Q$ -ERTM) method counteracts the subsurface quality-factor ( $Q$ ) filtering effect for attenuated multicomponent seismic data to produce high-quality migrated images. Compared with  $Q$ -compensated viscoacoustic reverse time migration ( $Q$ -ARTM),  $Q$ -ERTM provides more informative geologic and structural characterization of the subsurface, but it poses greater challenges on viscoelastic wavefield decomposition and stabilization. On the basis of our previously proposed stabilization operator for  $Q$ -ARTM, we have developed a mode-dependent adaptive stabilization scheme for  $Q$ -ERTM, which has the ability to handle the

numerical instability issue arising from viscoelastic compensation. The stabilization scheme exhibits superior properties of time variance and  $Q$  dependence over the commonly used low-pass filtering method. In the context of the viscoelastic wave equation with decoupled fractional Laplacians, we have thoroughly investigated the staggered-grid pseudospectral approach for viscoelastic simulation, vector-based wavefield decomposition for imaging, and mode-dependent adaptive stabilization for compensation. These indispensable modules eventually form the whole framework for stable and accurate  $Q$ -ERTM. The  $Q$ -ERTM results including PP- and PS-images from synthetic and field data sets are provided to verify the feasibility and superiority of our approach in terms of fidelity and stability.

### INTRODUCTION

Frequency-dependent amplitude absorption and phase-velocity dispersion are two kinds of typical phenomena that accompany seismic wave propagation through subsurface media. Such intrinsic quality-factor ( $Q$ ) filtering effects inevitably degrade the quality of seismograms, decrease the resolution of migrated images, and eventually affect the reliability of seismic interpretation. Early attempts to mitigate the  $Q$ -filtering effect are mainly performed on poststack seismic data and include time-varying deconvolution (Clarke, 1968; Griffiths et al., 1977; Margrave et al., 2011), time-variant spectral whitening (Yilmaz and Doherty, 2001), and inverse  $Q$  filtering (Hargreaves and Calvert, 1991; Wang, 2002, 2006; Wang et al., 2018b). In recent years, many researchers have paid considerable attention to investigate seismic-attenuation compensation during prestack migration (Mittet et al., 1995; Mittet, 2007; Zhang et al., 2012; Zhu et al.,

2014; Bai et al., 2016; Wang et al., 2018c, 2019), which is considered as a more physically consistent scheme due to the fact that amplitude attenuation and phase dispersion associated with anelasticity occur during wave propagation (Zhang et al., 2010; Zhu et al., 2014). Among these  $Q$ -compensated prestack migration methods,  $Q$ -compensated viscoacoustic reverse time migration ( $Q$ -ARTM) has attracted a lot of research interest in the geophysical community due to its high-fidelity imaging properties and broad prospects for application (Zhu et al., 2014; Guo et al., 2016; Wang et al., 2018c). Zhang et al. (2010) propose a  $Q$ -ARTM scheme based on a viscoacoustic wave equation involving a pseudodifferential operator to compensate for amplitude loss and phase-velocity dispersion. Inspired by the studies in medical photoacoustic tomography in medicine (Treeby and Cox, 2010; Treeby et al., 2010; Huang et al., 2012), Zhu and Harris (2014) develop a viscoacoustic wave equation with decoupled fractional Laplacians (DFLs) based on Kjartansson's constant- $Q$

Manuscript received by the Editor 31 May 2018; revised manuscript received 10 January 2019; published ahead of production 20 March 2019; published online 27 May 2019.

<sup>1</sup>State Key Lab of Petroleum Resources and Prospecting, Key Lab of Geophysical Exploration of CNPC, China University of Petroleum-Beijing, Changping, Beijing 102249, China. E-mail: helloworldyf@163.com; huizhou@cup.edu.cn (corresponding author); cupzhaoxuebin@qq.com.

<sup>2</sup>Chinese Academy of Geosciences, Center for Computational and Exploration Geophysics, State Key Laboratory of Geodesy and Earth's Dynamics, Institute of Geodesy and Geophysics, Xudong Road, Wuhan 430077, China. E-mail: zhqch2008.cool@163.com.

<sup>3</sup>Zhejiang University, School of Earth Sciences, Hangzhou 310027, China. E-mail: chenyk2018@126.com.

© 2019 Society of Exploration Geophysicists. All rights reserved.

model, and they further formulate the  $Q$ -ARTM framework based on this equation (Zhu et al., 2014). This equation is rather attractive for counteracting the  $Q$ -filtering effect during reverse time migration (RTM) due to its flexibility for separated amplitude recovery and phase correction. Although most recent efforts have been made to incorporate  $Q$ -ARTM for mitigating the subsurface attenuation effects on seismic imaging, to our knowledge, only a little attention has been paid to  $Q$ -compensated viscoelastic reverse time migration ( $Q$ -ERTM) (Deng and McMechan, 2008; Guo and McMechan, 2015; Zhu and Sun, 2017). This motivates some researchers to develop an accurate viscoelastic imaging approach that mitigates the effects of P- and S-wave attenuation. Deng and McMechan (2008) propose viscoelastic true-amplitude prestack RTM based on the generalized standard linear solid with multiple relaxation mechanisms, in which the intrinsic attenuation and its compensation are embedded in composite memory variables associated with relaxation mechanisms. Guo and McMechan (2015) and Zhu and Sun (2017) develop  $Q$ -ERTM in the context of the viscoelastic wave equation with DFLs, in which the separated attenuation compensation can be easily achieved by reversing the absorption proportionality coefficient in sign but leaving the equivalent dispersion parameter unchanged. Compared with  $Q$ -ARTM,  $Q$ -ERTM compensates the subsurface  $Q$ -filtering effects for attenuated multicomponent seismic data to produce high-quality migrated images. It has been proven that  $Q$ -ERTM can provide more informative geologic and structural characterization of the subsurface for seismic imaging and interpretation, but it poses greater challenges on viscoelastic wavefield decomposition and stabilization (Yan and Sava, 2008; Du et al., 2012; Zhu and Sun, 2017). More specifically,  $Q$ -ERTM constructs the vector wavefield using the viscoelastic wave equation and separates the coupled wavefield into P- and S-wave modes before applying an imaging condition. Furthermore, the seismic attenuation effect on P- and S-wave modes exhibits distinct properties of amplitude absorption and phase-velocity dispersion; thus, a mode-dependent stabilization scheme is required to obtain well-compensated PP- and PS-images.

Given the aforementioned situation, we focus on the numerical instability issue existing in  $Q$ -ERTM. It has been stated in many works that direct amplitude compensation will inevitably result in exponentially boosted high-frequency ambient noise (Zhu et al., 2014; Sun and Zhu 2015; Yang et al., 2016; Wang et al., 2017a, 2018c). By deriving Green's functions for the constant- $Q$  wave equation and its compensated equation, Wang et al. (2017c, 2018c) theoretically prove that the compensated constant- $Q$  equation is a heavily ill-posed equation due to the presence of the compensating term. The most intuitive method to overcome the instability is to apply a low-pass filter whose cutoff frequency is identified by the noise level of measured data to suppress the high-frequency component (Treeby et al., 2010; Ammari et al., 2013; Zhu et al., 2014). Such a time-invariant filtering approach maintains the fidelity of the compensated images within the filter's pass band, but it inevitably damages the high-frequency signal. Inspired by the fact that a signal loss manifests as a depth-dependent magnitude decrease and blurring of features within the recorded data, Treeby (2013) proposes a regularization scheme by using a time-variant window, whose cutoff frequency is based on the local time-frequency distribution of the recorded signal. Unlike the conventional low-pass filtering acting as a damage controller to suppress the high-frequency noise regardless of spatially varying  $Q$  and compensation depth (traveltimes), Wang et al. (2018c) develop an adaptive stabilization for  $Q$ -RTM, in which the stabiliza-

tion factor can be explicitly identified by the specified gain limit according to an empirical formula. In this paper, we generalize the previously developed adaptive stabilization scheme into a mode-dependent version for the viscoelastic situation, in which the P- and S-wave modes have distinct attenuating properties but similar forms of propagation equation.

In this study, we first describe the general principle of  $Q$ -ERTM in the framework of the viscoelastic wave equation with DFLs. Then, we thoroughly investigate some implementation details of  $Q$ -ERTM including the staggered-grid pseudospectral (SGPS) approach for viscoelastic extrapolation, vector-based wavefield decomposition for PP- and PS-imaging, and mode-dependent adaptive stabilization for P- and S-wave mode compensation. Following that, we perform  $Q$ -ERTM on synthetic and field data sets to demonstrate the stability and feasibility of the proposed mode-dependent adaptive stabilization scheme.

## GENERAL PRINCIPLE OF $Q$ -ERTM

### Viscoelastic wave equation with DFLs

We first introduce the general principle of  $Q$ -ERTM in the framework of constant- $Q$  wave equation with DFLs for the 2D case (Zhu and Carcione, 2014; Guo and McMechan, 2015; Wang et al., 2018a; Zhao et al., 2018), which can be recast as a first-order matrix differential equation of the following form:

$$\partial_t \mathbf{u}^\diamond = \mathbf{H} \mathbf{u}^\diamond + \mathbf{f}, \quad (1)$$

where  $\mathbf{u}^\diamond = (v_x, v_z, \sigma_{xx}, \sigma_{zz}, \sigma_{xz})^T$  is the  $5 \times 1$  unknown field array;  $\mathbf{f} = (f_x, f_z, 0, 0, 0)^T$  is the  $5 \times 1$  source array; and

$$\begin{aligned} \mathbf{H} = & \begin{pmatrix} 0 & 0 & 1/\rho\partial_x & 0 & 1/\rho\partial_z \\ 0 & 0 & 0 & 1/\rho\partial_z & 1/\rho\partial_x \\ (\eta_p \mathbf{D}_p + \tau_p \mathbf{A}_p \partial_t) \partial_x & \left( \eta_p \mathbf{D}_p - 2\eta_s \mathbf{D}_s + \right. \\ & \left. (\tau_p \mathbf{A}_p \partial_t - 2\tau_s \mathbf{A}_s \partial_t) \right) \partial_z & 0 & 0 & 0 \\ \eta_p \mathbf{D}_p - 2\eta_s \mathbf{D}_s + & (\tau_p \mathbf{A}_p \partial_t - 2\tau_s \mathbf{A}_s \partial_t) \partial_x & (\eta_p \mathbf{D}_p + \tau_p \mathbf{A}_p \partial_t) \partial_z & 0 & 0 \\ (\eta_s \mathbf{D}_s + \tau_s \mathbf{A}_s \partial_t) \partial_z & (\eta_s \mathbf{D}_s + \tau_s \mathbf{A}_s \partial_t) \partial_x & 0 & 0 & 0 \end{pmatrix} \\ = & \begin{pmatrix} 0 & 0 & 1/\rho\partial_x & 0 & 1/\rho\partial_z \\ 0 & 0 & 0 & 1/\rho\partial_z & 1/\rho\partial_x \\ (\bar{\lambda} + 2\bar{\mu}) \partial_x & \bar{\lambda} \partial_z & 0 & 0 & 0 \\ \bar{\lambda} \partial_x & (\bar{\lambda} + 2\bar{\mu}) \partial_z & 0 & 0 & 0 \\ \bar{\mu} \partial_z & \bar{\mu} \partial_x & 0 & 0 & 0 \end{pmatrix} \end{aligned} \quad (2)$$

denotes the spatial  $5 \times 5$  operator array. The terms  $\bar{\lambda}$  and  $\bar{\mu}$  in this operator represent the generalized Lamé coefficients under the viscoelastic case, which can be expressed as

$$\bar{\lambda} + 2\bar{\mu} = \eta_p \mathbf{D}_p + \tau_p \mathbf{A}_p \partial_t, \quad (3)$$

$$\bar{\Phi} = \eta_s \mathbf{D}_s + \tau_s \mathbf{A}_s \partial_t, \quad (4)$$

$$\bar{\lambda} = (\eta_p \mathbf{D}_p + \tau_p \mathbf{A}_p \partial_t) - 2(\eta_s \mathbf{D}_s + \tau_s \mathbf{A}_s \partial_t). \quad (5)$$

There are two fractional Laplacians in these coefficients, i.e.,

$$\mathbf{D}_m = (-\nabla^2)^{\gamma_m}, \quad \mathbf{A}_m = (-\nabla^2)^{\gamma_m-1/2}, \quad m = P, S, \quad (6)$$

which are, respectively, responsible for the phase velocity dispersion and amplitude attenuation. The subscript  $m = P, S$  represents the P- or S-wave. The proportionality coefficients of two fractional Laplacians are given by

$$\eta_m = C_m c_{m_0}^{2\gamma_m} \cos(\pi\gamma_m), \quad \tau_m = C_m c_{m_0}^{2\gamma_m-1} \sin(\pi\gamma_m), \quad (7)$$

where

$$C_m = \rho c_{m_0}^2 \cos^2[\pi\gamma_m/2] \omega_0^{-2\gamma_m}, \quad m_0 = P_0, S_0, \quad (8)$$

and the dimensionless parameter  $\gamma_m = \arctan(1/\pi Q_m)$  range within (0, 1/2) for any positive values of  $Q_m$ . The terms  $c_{P_0}$  and  $c_{S_0}$  denote the P- and S-wave velocity at the reference frequency  $\omega_0$ . For lossless media, as  $Q \rightarrow \infty, \gamma \rightarrow 0$ , so  $\eta \rightarrow -1$  and  $\tau \rightarrow 0$ , then we have

$$\bar{\lambda} + 2\bar{\Phi} = \rho c_p^2 = \lambda + 2\mu, \quad \bar{\Phi} = \rho c_s^2 = \mu, \quad (9)$$

which indicates that the spatial operator  $\mathbf{H}$  can be reduced to the elastic case.

### The SGPS method for viscoelastic simulation

In this subsection, we aim to develop a computationally efficient numerical method for solving equation 1, in which the first-order spatial derivatives and fractional Laplacians are involved. The SGPS method, which represents an extension of the SGFD method, can help to reduce the requirement that many grid points per wavelength are needed to overcome the spatial dispersion. The spatial operator  $\mathbf{H}$  in equation 1 can be further decomposed into two parts as

$$\mathbf{H} = \begin{pmatrix} \mathbf{0} & \boldsymbol{\Phi} \\ \boldsymbol{\Psi} & \mathbf{0} \end{pmatrix}, \quad (10)$$

where  $\boldsymbol{\Phi}$  and  $\boldsymbol{\Psi}$ , represented as  $3 \times 2$  array and  $2 \times 3$  array, separately denote the spatial operators acting on the stress and particle velocity field. Thus, the viscoelastic wave equation 1 can be discretized as

$$\mathbf{v}^+ = \mathbf{v}^- + \frac{\Delta t}{\rho} \boldsymbol{\Phi} \boldsymbol{\sigma}^- \quad (11)$$

and

$$\boldsymbol{\sigma}^+ = \boldsymbol{\sigma}^- + \Delta t \boldsymbol{\Psi} \mathbf{v}^+, \quad (12)$$

where  $\mathbf{v}^+ = (v_x^+, v_z^+)^T$  and  $\mathbf{v}^- = (v_x^-, v_z^-)^T$  are the velocity  $2 \times 1$  field array and  $\boldsymbol{\sigma}^+ = (\sigma_{xx}^+, \sigma_{zz}^+, \sigma_{xz}^+)^T$  and  $\boldsymbol{\sigma}^- = (\sigma_{xx}^-, \sigma_{zz}^-, \sigma_{xz}^-)^T$  are the stress  $3 \times 1$  field array. The superscripts + and - on the velocity

and stress field denote the corresponding field at current and previous time steps, respectively. According to the SGPS method, the first-order spatial derivatives can be calculated as

$$\partial_{j^\pm} = \mathcal{F}_j^{-1}\{ik_j e^{\pm ik_j \Delta j / 2} \mathcal{F}_j\} = \mathcal{F}_j^{-1}\{ik_j^\pm \mathcal{F}_j\}, \quad (13)$$

where  $\mathcal{F}_j$  and  $\mathcal{F}_j^{-1}$  denote the 1D Fourier transform and 1D inverse Fourier transform along the  $j$ th axis. The term  $i = \sqrt{-1}$  is the imaginary unit,  $|\mathbf{k}| = \sqrt{k_x^2 + k_z^2}$  denotes the norm of the vector wavenumber, and  $k_j$  is the discrete wavenumber along the  $j$ th dimension. The superscripts + and - on wavenumber  $k_j$  denote a spatial shift that translates the output by left (up) and right (down) with half the spatial interval, respectively. Fractional Laplacians in operator 2 can be efficiently calculated as

$$\begin{aligned} \mathbf{D}_m[\partial_{j^\pm}] &= \mathcal{F}^{-1}\{|\mathbf{k}|^{2\gamma_m} \mathcal{F}[\partial_{j^\pm}]\} \\ &= \mathcal{F}^{-1}\{|\mathbf{k}|^{2\gamma_m} \mathcal{F}_{l \neq j}[ik_j^\pm \mathcal{F}_j]\} \\ &= \mathcal{F}^{-1}\{|\mathbf{k}|^{2\gamma_m} ik_j^\pm \mathcal{F}_j\}, \\ &= \mathcal{F}^{-1}\{|\mathbf{k}|^{2\gamma_m-1} \mathcal{F}_{l \neq j}[ik_j^\pm \mathcal{F}_j]\} \\ &= \mathcal{F}^{-1}\{|\mathbf{k}|^{2\gamma_m-1} \mathcal{F}_{l \neq j}[ik_j^\pm \mathcal{F}_j]\} \\ &= \mathcal{F}^{-1}\{|\mathbf{k}|^{2\gamma_m-1} ik_j^\pm \partial_t \mathcal{F}_j\}, \end{aligned} \quad (14)$$

where  $\mathcal{F}$  and  $\mathcal{F}^{-1}$  denote the 2D Fourier transform and 2D inverse Fourier transform. Owing to the fact that 2D Fourier transform can be considered as performing 1D Fourier transform twice along each dimension, we can reduce the computational cost of two 1D inverse Fourier transforms during each calculation of the fractional Laplacian. As shown in equation 14, the 2D Fourier transform operator  $\mathcal{F}$  can be obtained by performing a 1D Fourier transform  $\mathcal{F}_{l \neq j}$  on the operator  $ik_j^\pm \mathcal{F}_j$  along the  $l$ th dimension. According to equations 13 and 14, the discrete spatial operators  $\boldsymbol{\Phi}$  and  $\boldsymbol{\Psi}$  in equations 11 and 12 can be finally expressed as

$$\boldsymbol{\Phi} = \begin{pmatrix} 1/\rho \mathcal{F}_x^{-1}\{ik_x^+ \mathcal{F}_x\} & 0 & 1/\rho \mathcal{F}_z^{-1}\{ik_z^- \mathcal{F}_z\} \\ 0 & 1/\rho \mathcal{F}_z^{-1}\{ik_z^+ \mathcal{F}_z\} & 1/\rho \mathcal{F}_x^{-1}\{ik_x^- \mathcal{F}_x\} \end{pmatrix}, \quad (15)$$

and

$$\boldsymbol{\Psi} = \begin{pmatrix} \eta_p \mathbf{D}_p[\partial_{x^-}] + \tau_p \mathbf{A}_p[\partial_{x^-}] & \eta_p \mathbf{D}_p[\partial_{z^-}] + \tau_p \mathbf{A}_p[\partial_{z^-}] \\ \eta_p \mathbf{D}_p[\partial_{x^-}] + \tau_p \mathbf{A}_p[\partial_{x^-}] & \eta_p \mathbf{D}_p[\partial_{z^-}] + \tau_p \mathbf{A}_p[\partial_{z^-}] \\ -2(\eta_s \mathbf{D}_s[\partial_{x^-}] + \tau_s \mathbf{A}_s[\partial_{x^-}]) & \eta_s \mathbf{D}_s[\partial_{x^+}] + \tau_s \mathbf{A}_s[\partial_{x^+}] \\ \eta_s \mathbf{D}_s[\partial_{x^-}] + \tau_s \mathbf{A}_s[\partial_{x^-}] & \eta_s \mathbf{D}_s[\partial_{x^+}] + \tau_s \mathbf{A}_s[\partial_{x^+}] \end{pmatrix}, \quad (16)$$

where  $\mathbf{D}_m[\partial_{j^\pm}]$  and  $\mathbf{A}_m[\partial_{j^\pm}]$  are defined in equation 14. As we can see from the discrete spatial operators  $\boldsymbol{\Phi}$  and  $\boldsymbol{\Psi}$ , a large number of 1D and 2D Fourier transforms are involved during the viscoelastic simulation, which incur the most computational cost compared with the rest of the simulation parts. For an intuitive understanding, we estimate the total 1D and 2D fast Fourier transforms (FFTs) and the corresponding inverse FFTs (IFFTs) used in the numerical simulation in equation 1. For calculating the velocity field using equation 11, four 1D FFTs and four 1D IFFTs are required; for solving the stress field using equation 12, two 2D FFTs and 12 2D IFFTs are required.

## Wavefield decomposition and viscoelastic imaging condition

In this part, we intend to formulate the viscoelastic imaging condition for  $Q$ -ERTM. Viscoelastic extrapolation couples the

P- and S-wave components and further suffers from seismic attenuation and dispersion effects when propagating through subsurface media. Therefore, three indispensable steps are involved for achieving viscoelastic imaging: wavefield decomposition, attenuation compensation, and imaging.

We first introduce a P- and S-wavefield decomposition method for viscoelastic extrapolation. In multicomponent seismic data, P- and S-wave modes exist in each particle-velocity component. As we know, it will inevitably bring crosstalk artifacts between different wave modes when the unseparated wavefield is directly introduced into the migration procedure. The earlier attempts to separate the P- and S-wave components are based on the Helmholtz theory that introduces divergence and curl operators (Dellinger and Etgen, 1990; Yan and Sava, 2008; Du et al., 2012). However, such a scalar separation scheme might cause an unwanted amplitude change and polarity reversal, which degrades the quality of the imaging results by destroying their original physical meaning. In recent years, a vector-based wavefield decomposition method has been proposed to keep the exact vector property of the coupled wavefield (Zhang et al., 2007, 2017; Xiao and Leaney, 2010; Wang et al., 2015; Chen et al., 2017; Du et al., 2017; Zhao et al., 2018). Here, we conduct P- and S-wavefield decomposition by introducing the P-wave stress variable  $\sigma_p$  and S-wave stress variable  $\sigma_s$ . The detailed viscoelastic wavefield-decomposition process is presented in Appendix A. The decomposed viscoelastic wave equation can be expressed as

$$\partial_t \mathbf{u}^\circ = \mathbf{W} \mathbf{u}^*, \quad (17)$$

where  $\mathbf{u}^\circ = (\sigma_p, v_{xp}, v_{zp}, \sigma_s, v_{xs}, v_{zs})^T$  is the  $6 \times 1$  decomposed wavefield array;  $\mathbf{u}^* = (v_x, v_z, \sigma_p, \sigma_s)^T$  is the  $4 \times 1$  hybrid wavefield array; and

$$\mathbf{W} = \begin{pmatrix} (\bar{\lambda} + 2\bar{\mu})\partial_x & \bar{\lambda}\partial_z & 0 & 0 \\ 0 & 0 & 1/\rho\partial_x & 0 \\ 0 & 0 & 1/\rho\partial_z & 0 \\ \bar{\mu}\partial_z & -\bar{\mu}\partial_x & 0 & 0 \\ 0 & 0 & 0 & 1/\rho\partial_z \\ 0 & 0 & 0 & -1/\rho\partial_x \end{pmatrix}, \quad (18)$$

denotes the  $6 \times 4$  decomposed spatial operator array. The subscripts  $p$  and  $s$  on the velocity field denote the pure P- and S-particle-velocity component, and we have  $v_x = v_{xp} + v_{xs}$  and  $v_z = v_{zp} + v_{zs}$ . Equations 1 and 17 provide a complete framework for viscoelastic wavefield extrapolation and decomposition. We can discretize equation 17 via the SGPS scheme in a similar way as that for equation 1, which brings extra computational cost of four 1D FFTs and four 1D IFFTs. The discrete spatial operator  $\mathbf{W}$  is given by

$$\mathbf{W} = \begin{pmatrix} \eta_p \mathbf{D}_p[\partial_x^-] + \tau_p \mathbf{A}_p[\partial_x^-] & \eta_p \mathbf{D}_p[\partial_z^-] + \tau_p \mathbf{A}_p[\partial_z^-] & 0 & 0 \\ 0 & 0 & 1/\rho \mathcal{F}_z^{-1}\{ik_x^+ \mathcal{F}_x\} & 0 \\ 0 & 0 & 1/\rho \mathcal{F}_z^{-1}\{ik_z^+ \mathcal{F}_z\} & 0 \\ \eta_s \mathbf{D}_s[\partial_z^+] + \tau_s \mathbf{A}_s[\partial_z^+] & -\eta_s \mathbf{D}_s[\partial_x^+] - \tau_s \mathbf{A}_s[\partial_x^+] & 0 & 0 \\ 0 & 0 & 0 & 1/\rho \mathcal{F}_z^{-1}\{ik_z^- \mathcal{F}_z\} \\ 0 & 0 & 0 & -1/\rho \mathcal{F}_x^{-1}\{ik_x^- \mathcal{F}_x\} \end{pmatrix}. \quad (19)$$

Another issue is the attenuation compensation during the viscoelastic extrapolation. Equations 1 and 17 seem to be attractive for Q-ERTM owing to their flexibility for separately compensating amplitude loss and correcting phase distortion. As stated by Treeby et al. (2010) and Zhu et al. (2014), the attenuation compensation for the equation with DFLs can be easily achieved by reversing the absorption proportionality coefficient in sign but leaving the equivalent dispersion parameter unchanged. In other words, compensated viscoelastic extrapolation can be performed by reversing the term  $\tau_m$  in the spatial operators  $\mathbf{H}$  (equation 2) and  $\mathbf{W}$  (equation 18) in sign. Here, we define the compensated spatial operators as  $\mathbf{H}^c$  and  $\mathbf{W}^c$ , and the compensated viscoelastic wave equations are given by

$$\partial_t \mathbf{u}^\circ c = \mathbf{H}^c \mathbf{u}^\circ c + \mathbf{f} \quad (20)$$

and

$$\partial_t \mathbf{u}^\circ c = \mathbf{W}^c \mathbf{u}^\bullet c, \quad (21)$$

where the superscript  $c$  of the wavefield variables stands for the compensated wavefield.

Because we have formulated the compensated viscoelastic wave equations 20 and 21, the viscoelastic imaging condition with  $Q$ -compensation can be further obtained. In this paper, source-normalized crosscorrelation imaging conditions in the inner product form are adopted for vector-based viscoelastic imaging. They are given by

$$\begin{aligned} I_{pp}(\mathbf{x}) &= \frac{\int_0^T \mathbf{v}_p^{Sa}(\mathbf{x}, t) \cdot \mathbf{v}_p^{Rc}(\mathbf{x}, t) dt}{\int_0^T \mathbf{v}_p^{Sa}(\mathbf{x}, t) \cdot \mathbf{v}_p^{Sa}(\mathbf{x}, t) dt}, \\ I_{ps}(\mathbf{x}) &= \frac{\int_0^T \mathbf{v}_p^{Sa}(\mathbf{x}, t) \cdot \mathbf{v}_s^{Rc}(\mathbf{x}, t) dt}{\int_0^T \mathbf{v}_p^{Sa}(\mathbf{x}, t) \cdot \mathbf{v}_p^{Sa}(\mathbf{x}, t) dt}, \end{aligned} \quad (22)$$

where superscripts  $S$  and  $R$  denote the source and receiver wavefields, respectively. Superscript  $a$  of the superscript  $S$  denotes the attenuated source wavefield, and superscript  $c$  of the superscript  $R$  denotes the  $Q$ -compensated receiver wavefield (Sun and Zhu, 2015; Zhu, 2016). However, amplitude compensation during time-reverse viscoelastic extrapolation is a nonstationary process with energy exponentially amplified over traveltime, which indeed boosts high-frequency ambient noise and even results in numerical instability. In the next section, we develop a novel stabilization scheme for  $Q$ -ERTM, thereby generating higher resolution and higher fidelity images.

## MODE-DEPENDENT ADAPTIVE STABILIZATION FOR $Q$ -ERTM

We have overviewed the general principle of  $Q$ -ERTM and also provided some technical details for viscoelastic extrapolation, decomposition, and compensation. Mathematically speaking, compensated viscoelastic wave equations 20 and 21 are severely ill posed due to the presence of amplitude-compensating terms in spatial operators  $\mathbf{H}^c$  and  $\mathbf{W}^c$ . Wang et al. (2018c) propose an adaptive stabilization operator for  $Q$ -ARTM by analytically deriving the Green's functions for the constant- $Q$  wave equation and its compensated equation. Here, we first give a brief recall of adaptive stabilization for  $Q$ -ARTM and then we develop a mode-based adaptive stabilization for  $Q$ -ERTM.

Inspired by the work of Wang (2006), Wang et al. (2018c) propose a similar adaptive stabilization for  $Q$ -RTM. The stabilization operator for viscoacoustic  $Q$ -RTM can be expressed as

$$\Upsilon(\mathbf{k}, l\Delta t) = \begin{cases} \frac{1}{1+\sigma^2 e^{2\xi_2(\mathbf{k})\Delta t}}, & l = 1, \\ \frac{1}{1+\sigma^2 e^{2\xi_2(\mathbf{k})(l-1)\Delta t}}, & l = 2, 3, \dots, n, \end{cases} \quad (23)$$

where the parameter  $\xi_2(\mathbf{k}) = -\tau c^2 |\mathbf{k}|^{2\gamma+1}/2 > 0$  is the imaginary part of the solution of the dispersion relation (Sun et al., 2014; Wang et al., 2018c). The stabilization factor  $\sigma^2$  can be empirically obtained from a specific gain limit  $G_{\lim}$ ,

$$\sigma^2 = e^{-0.23G_{\lim}-1.39}. \quad (24)$$

The Green's function of the compensated equation is divergent at the high-wavenumber end, which eventually results in numerical instability during compensation. That is to say, attenuating media can be considered as a time-variant system with seismic wave energy exponentially decreasing; contrarily, attenuation compensation is a nonstationary process with the energy exponentially amplified over the propagation time. Furthermore, the exponentially decreased or increased degree is closely linked to the magnitude of the wavenumber  $|\mathbf{k}|$ , which suggests that the high-wavenumber components are more vulnerable to be absorbed or amplified. To illustrate the inherent adaptability of such a stabilization scheme, we numerically compare the compensated time propagator (Figure 1a) and stabilized time propagators using low-pass filtering (Figure 1b) and our proposed scheme (Figure 1c). We set  $\sigma^2 = 2.5 \times 10^{-7}$  for our proposed method, and we use the cutoff wavenumber  $\rho = 0.16 \text{ m}^{-1}$  for the low-pass filter. From Figure 1b and 1c, we can conclude that our proposed stabilization scheme preserves more high-wavenumber components at an earlier propagation time and it prevents the propagator from being unstable by suppressing high-wavenumber components at a later time; whereas, low-pass filtering may result in high-wavenumber loss in a short period of time, and relatively high-wavenumber divergence over a long period of time. Moreover, seismic attenuation compensation with adaptive stabilization exhibits su-

prior property of time variance and  $Q$  dependence because the stabilized gain curve is automatically adjusted with traveltime  $t$  and quality factor  $Q$ . Therefore, it can intelligently avoid boosting the ambient noise, especially for noisy data.

We have briefly revisited our previously proposed adaptive stabilization scheme for  $Q$ -ARTM, which can be considered as the stabilization operator  $\Upsilon(\mathbf{k}, l\Delta t)$  acting on the P-wave mode. Here, we generalize this stabilization scheme to the S-wave mode and then develop a mode-based adaptive stabilization for  $Q$ -ERTM. The numerical model described in this paper is based on the first-order equation 1; however, the adaptive stabilization scheme is derived from the second-order wave equation, which can be obtained by eliminating the stress tensor from equation 1. In homogeneous

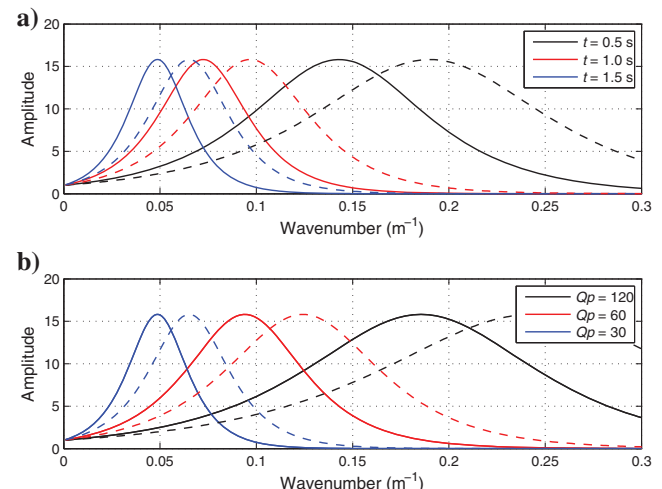


Figure 2. The stabilized compensation coefficients  $\Delta(\mathbf{k}, t)$  varying with (a) different traveltimes  $t = 0.5, 1.0, \text{ and } 1.5 \text{ s}$  ( $Q_p = 30$  and  $\sigma^2 = 0.1\%$ ), (b) different quality factor  $Q_p = 120, 60, \text{ and } 30$  ( $t = 1.5$  and  $\sigma^2 = 0.1\%$ ), where the solid lines represent a P-wave and the dashed lines represent an S-wave. For simplicity, we set  $c_p/c_s = 1.7$  and  $Q_p/Q_s = 1.3$  for this synthetic example.

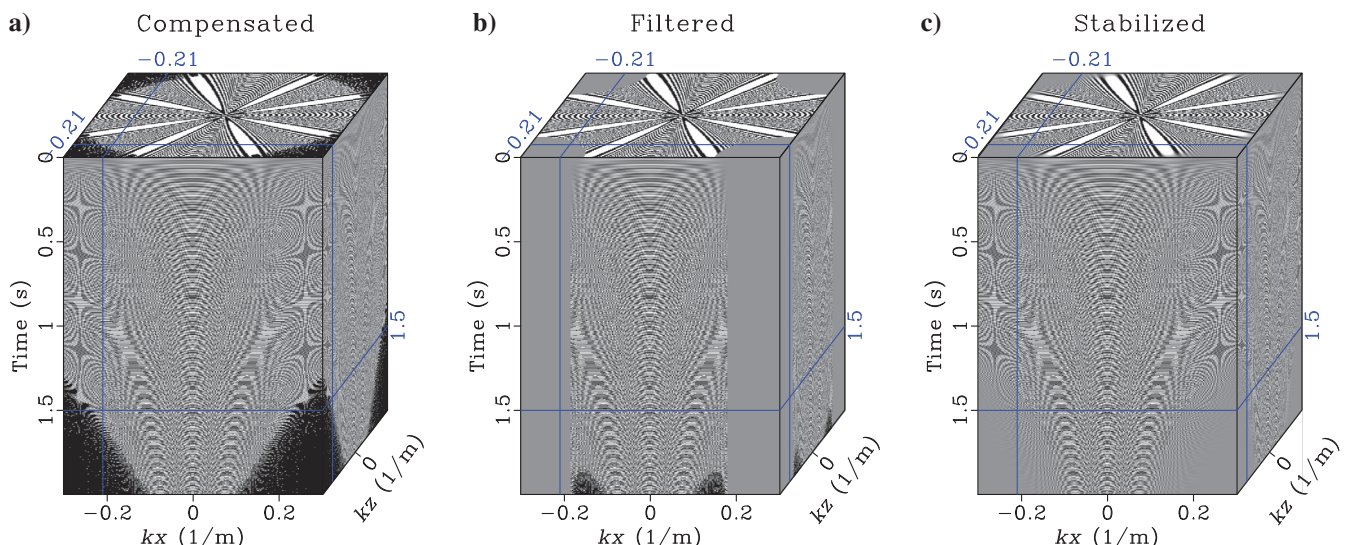


Figure 1. (a) The compensated time propagator and stabilized time propagators using (b) low-pass Tukey filtering and (c) the proposed adaptive stabilization. We clip the same amplitude value for these three figures.

media, using the vector notation with  $\mathbf{u} = (u_x, u_z)$ , the second-order viscoelastic wave equation has the following form:

$$\rho \frac{\partial^2 \mathbf{u}}{\partial t^2} - (\eta_p \mathbf{D}_p + \tau_p \mathbf{A}_p \partial_t) \nabla (\nabla \cdot \mathbf{u}) + (\eta_s \mathbf{D}_s + \tau_s \mathbf{A}_s \partial_t) \nabla \times (\nabla \times \mathbf{u}) = \mathbf{0}, \quad (25)$$

where the forcing term has been left out for simplicity. According to Helmholtz's theorems, we can write the displacement as the sum of the gradient of a scalar potential and the curl of a vector potential,

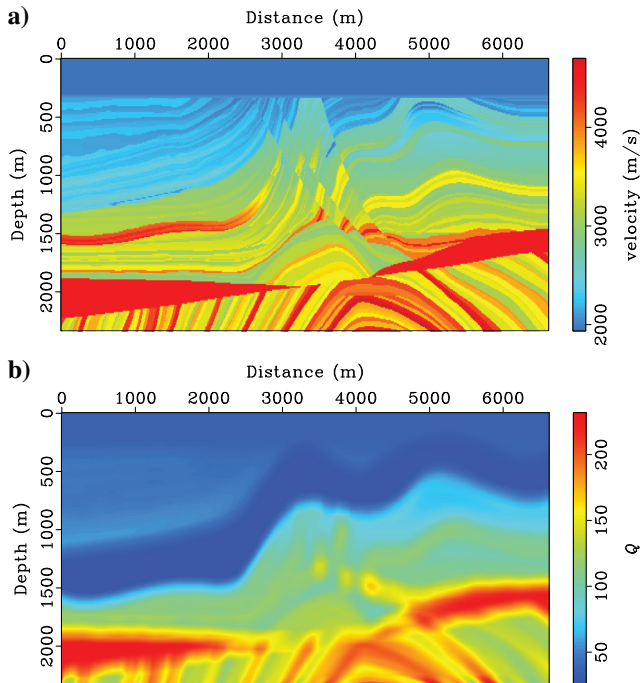


Figure 3. (a) The P-wave velocity and (b)  $Q_p$  of the Marmousi model, and S-wave velocity  $c_s$  and S-wave quality factor  $Q_s$  are obtained by setting  $c_p/c_s = 1.7$  and  $Q_p/Q_s = 1.3$ .

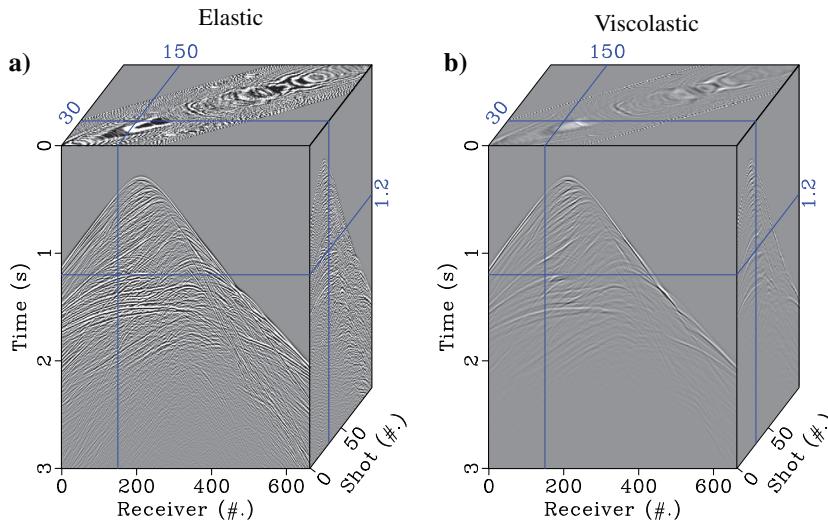


Figure 4. Synthetic vertical-component seismogram obtained from (a) elastic and (b) viscoelastic modeling. We clip the same amplitude value for these two figures.

$$\mathbf{u} = \mathbf{u}_p + \mathbf{u}_s = \nabla \phi + \nabla \times \psi, \quad (26)$$

where  $\mathbf{u}_p = \nabla \phi$  and  $\mathbf{u}_s = \nabla \times \psi$  are the compressional and shear components of the displacement. Therefore, the vector equation 25 can be split into two parts corresponding to P- and S-wave propagation:

$$\rho \frac{\partial^2 \mathbf{u}_p}{\partial t^2} - (\eta_p \mathbf{D}_p + \tau_p \mathbf{A}_p \partial_t) \nabla (\nabla \cdot \mathbf{u}_p) = 0 \quad (27)$$

and

$$\rho \frac{\partial^2 \mathbf{u}_s}{\partial t^2} + (\eta_s \mathbf{D}_s + \tau_s \mathbf{A}_s \partial_t) \nabla \times (\nabla \times \mathbf{u}_s) = \mathbf{0}. \quad (28)$$

From the viscoelastic equations 27 and 28, we can conclude that the P- and S-wave modes satisfy a unified form. Therefore, the mode-dependent adaptive stabilization can be given as

$$\Upsilon_m(\mathbf{k}, l\Delta t) = \begin{cases} \frac{1}{1+\sigma^2 e^{2\xi_m(\mathbf{k})\Delta t}}, & l = 1, \\ \frac{1+\sigma^2 e^{2\xi_m((l-1)\Delta t)}}{1+\sigma^2 e^{2\xi_m(\mathbf{k})\Delta t}}, & l = 2, 3, \dots, n, \end{cases} \quad (29)$$

where the exponential term  $\xi_m(\mathbf{k})$  controls the stabilizing effects on the P- and S-wave modes, which is defined as

$$\xi_m(\mathbf{k}) = c_{p0,s0}^{2\gamma_m+1} \omega_0^{-2\gamma_m} \sin(\pi\gamma_m) \cos^2(\pi\gamma_m/2) |\mathbf{k}|^{2\gamma_m+1}/2. \quad (30)$$

To verify the fact that the P- and S-wave modes require mode-dependent stabilization due to their distinct attenuating properties, we plot the viscoelastic compensation curves  $\Lambda(\mathbf{k}, t)$  at a different traveltime  $t$  (Figure 2a) and with a different quality factor  $Q_m$  (Figure 2b), in which the solid lines represent a P-wave and the dashed lines represent an S-wave. We assume that the reference P-wave velocity  $c_{p0}$  of the homogeneous medium is 3000 m/s. For simplicity, we set  $c_p/c_s = 1.7$  and  $Q_p/Q_s = 1.3$  for all synthetic examples in this paper. Figure 2a shows the P- and S-wave gain curves at  $t = 0.5, 1.0$ , and  $1.5$ s, respectively, with  $Q_p = 30$

and  $\sigma^2 = 0.1\%$ . These curves have the same peak amplitude value but a different frequency band range. More specifically, the effective compensation range shifts to the low frequencies and becomes narrow with time and the S-wave gain curves have a wider compensation range overall than that of the P-wave gain curves. From Figure 2b, we can draw a similar conclusion that the compensation curves move toward the low frequencies as the  $Q$ -value decreases. In general, the rules of stabilized compensation curves varying with traveltime  $t$  and quality factor  $Q_m$  agree with our intuitive understanding. Considering seismic wave propagation in high-attenuation media with smaller  $Q_m$ , when it travels a longer time, its amplitude undergoes more intensive attenuation, especially at the high-frequency components; accordingly,  $Q$ -compensation tends to drastically amplify such an attenuated signal even ambient noise, whereas an amplitude-compensation operator with stabilization can adaptively avoid boosting the ambient noise by high-frequency

suppression. Furthermore, the S-wave has a relatively shorter wavelength than the P-wave, which leads to the wider compensation range for the S-wave mode. Consequently, it indicates that our proposed stabilization is an adaptive scheme adapted well to  $Q$ -ERTM.

## NUMERICAL EXAMPLES

Compared to conventional  $Q$ -ERTM stabilized by a low-pass filter, our proposed  $Q$ -ERTM with mode-dependent adaptive stabilization can theoretically recover as many high-frequency components of shallow structures as possible while maintaining a relatively stable compensation for deep structures. In this section, we perform  $Q$ -ERTM on a synthetic data set, respectively, stabilized by low-pass filtering and our proposed method, to demonstrate the superiority

of the proposed approach in terms of fidelity and stability. All of the numerical examples are conducted by CUDA programming on the Tesla K10 GPU cluster. We adopt a checkpointing-assisted time-reversal reconstruction scheme to reconstruct the source wave-fields, which combines the efficiency of reverse propagation and the stability of checkpointing (Yang et al., 2016; Wang et al., 2017b).

## $Q$ -ERTM for the synthetic data

We conduct  $Q$ -ERTM for the Marmousi model, whose P-wave velocity and  $Q_p$  models are, respectively, shown in Figure 3a and 3b, respectively. As we have mentioned above, we set  $c_p/c_s = 1.7$  and  $Q_p/Q_s = 1.3$  for this synthetic example. A high-attenuation zone with a low value of  $Q_p = 30$  is located at the dark-blue zone

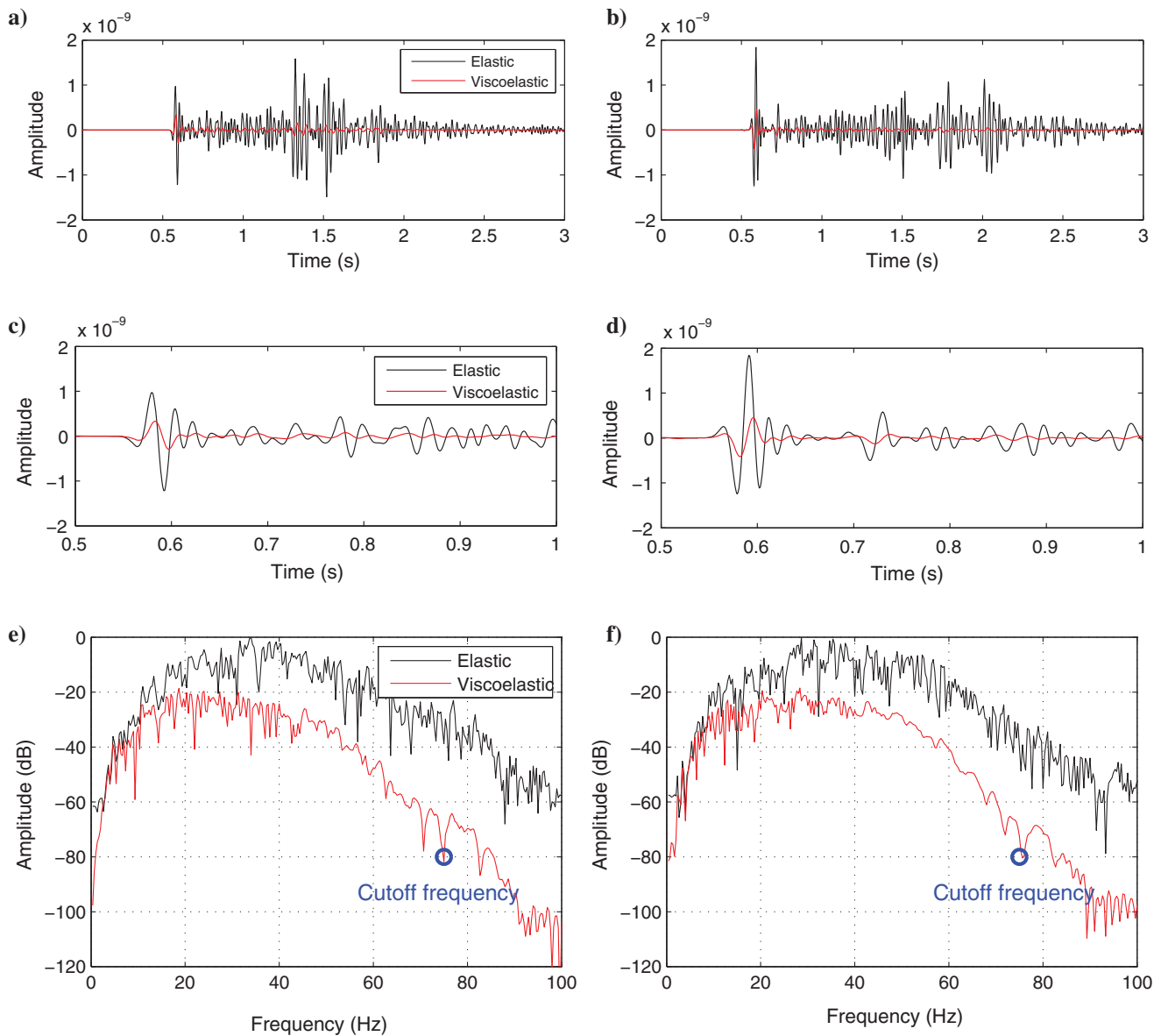


Figure 5. Synthetic traces selected arbitrarily at a distance of 3 km from the 30th shot, (a) vertical component and (b) horizontal component of the original and attenuated seismogram, (c) magnified view of the vertical component, (d) magnified view of the horizontal component, and the corresponding amplitude spectra (e and f). In each figure, the black line corresponds to the elastic data without attenuation and the red line corresponds to the attenuated data.

in Figure 3b, which distributes at approximately 1400 m in depth on the left and shallows to 500 m on the right. The size of the model is  $6.63 \times 2.34$  km with grid spacing of  $dx = dz = 10$  m. In the obser-

vation system, there are 100 shots distributed laterally with a shot interval of  $ds = 60$  m, and each of them is accompanied with 201 double-sided receivers. The source function is a Ricker wavelet with

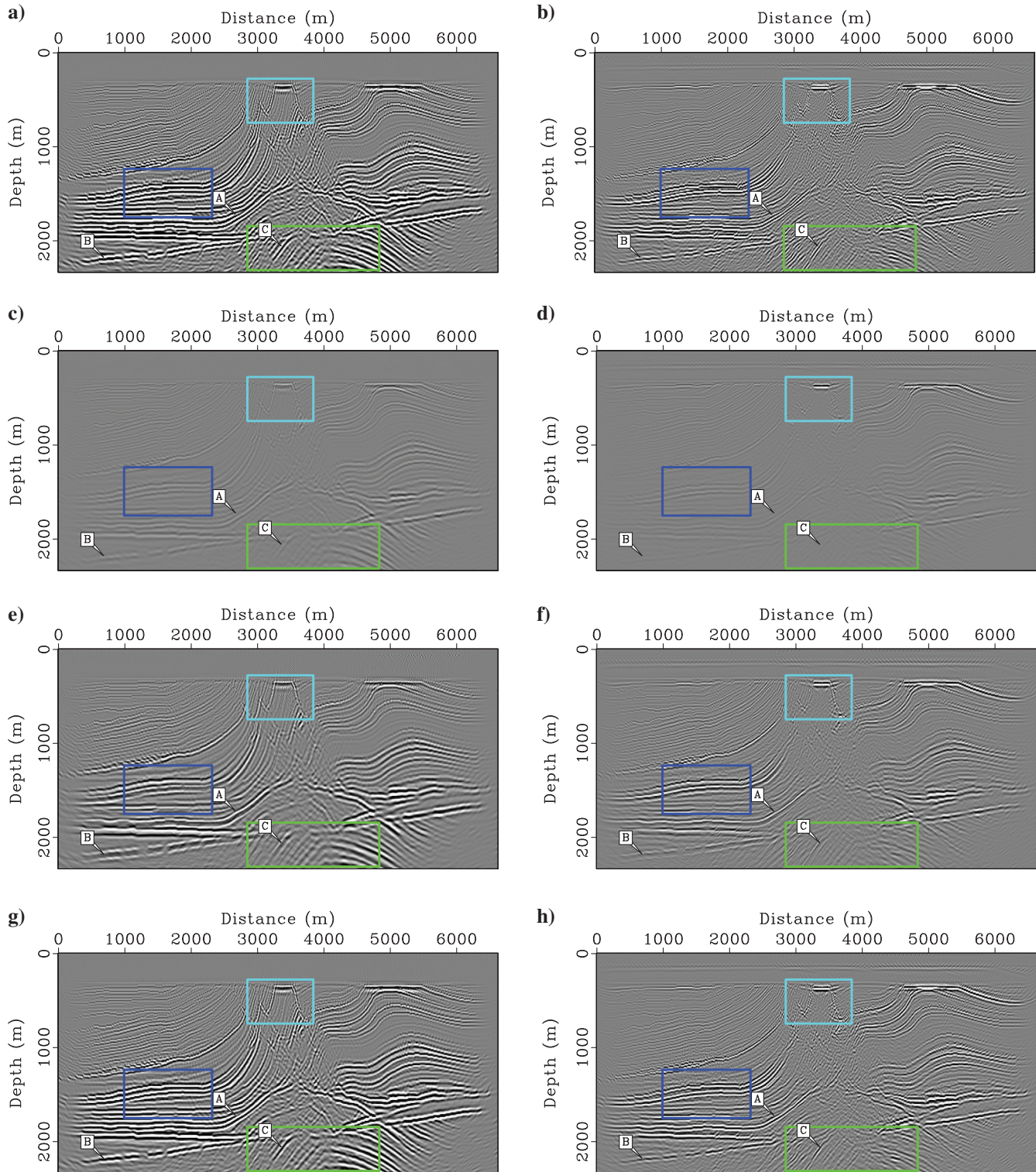


Figure 6. Migrated images of the Marmousi model obtained by (a and b) elastic RTM, (c and d) elastic RTM on lossy data, (e and f) low-pass-filtered Q-ERTM, and (g and h) adaptively stabilized Q-ERTM. The left column (a, c, e, and g) shows the PP-images, and right column (b, d, f, and h) shows the PS-images. The labels A, B, and C denote the three reflectors below the high-attenuation zone.

a dominant frequency  $f_d = 30$  Hz. The synthetic seismic data are modeled by the  $k$ -SGPS with time interval  $dt = 0.001$  s, and the seismic records last 3.0 s.

To identify a reasonable cutoff frequency for the conventional filtered Q-ERTM and the stabilization factor for our proposed stabilized Q-ERTM, we need to estimate the attenuation level of the measured data (Zhu et al., 2014; Wang et al., 2018c). Figure 4a and 4b shows synthetic vertical-component seismograms in elastic and viscoelastic media, respectively. We can observe the apparent amplitude decay from the viscoelastic gather, especially for far-offset reflections. Figure 5a and 5b displays traces selected arbitrarily at the distance of 3 km from the vertical and horizontal components of the 30th shot gathers, which exhibit apparent an amplitude difference between these two traces. Figure 5c and 5d presents magnified views of these traces, which show slight phase dislocation between these two traces. The corresponding power spectra are shown in Figure 5e and 5f, from which we select the cutoff frequency of 75 Hz for the Tukey filter (the blue circle marked in Figure 5e and 5f). The cutoff frequency  $f_c$  is calculated by multiplying the cutoff wavenumber  $k_c$  by the mean velocity  $c_{\text{mean}}$  of the model. To conduct a fair comparison between the low-pass filtering method and our proposed adaptive-stabilization scheme, we need to select the cutoff frequency  $f_c$  and stabilization factor  $\sigma^2$  under a relatively

consistent criterion. In this synthetic example, we adopt the gain limit  $G_{\lim}$  of 80 dB (corresponds to stabilization factor  $\sigma^2 = 2.5 \times 10^{-8}$ ) for our proposed stabilized Q-ERTM to alleviate numerical instability, which is nearly equivalent to the conventional filtering method with the cutoff frequency  $f_c = 75$  Hz at a reference propagation time  $t_0 = 1.0$  s. It is remarkable that the mode-dependent adaptive stabilization scheme imposes distinct amplitude suppression for P- and S-wave during viscoelastic wavefield reconstruction and compensation, even though they have the same stabilization factor.

Figure 6 shows the migrated PP- and PS-images (Figure 6a and 6b) using the conventional ERTM from lossless seismic data and the PP- and PS-images (Figure 6c and 6d) using the attenuated seismic data, low-pass filtered Q-ERTM images (Figure 6e and 6f) from the attenuated seismic data, and our proposed adaptively stabilized Q-ERTM images (Figure 6g and 6h) from the attenuated seismic data, respectively. In this example, the ERTM results shown in Figure 6a and 6b serve as the ideal reference for the comparison of the compensation performance. Due to the presence of a high-attenuation zone, the imaging results of the structure beneath the high-attenuation zone shown in the blue frame in Figure 6c and 6d exhibit attenuated amplitudes and blurred structures; besides, it also gravely affects the migration image of the anticinal structure shown in the green frames in Fig-

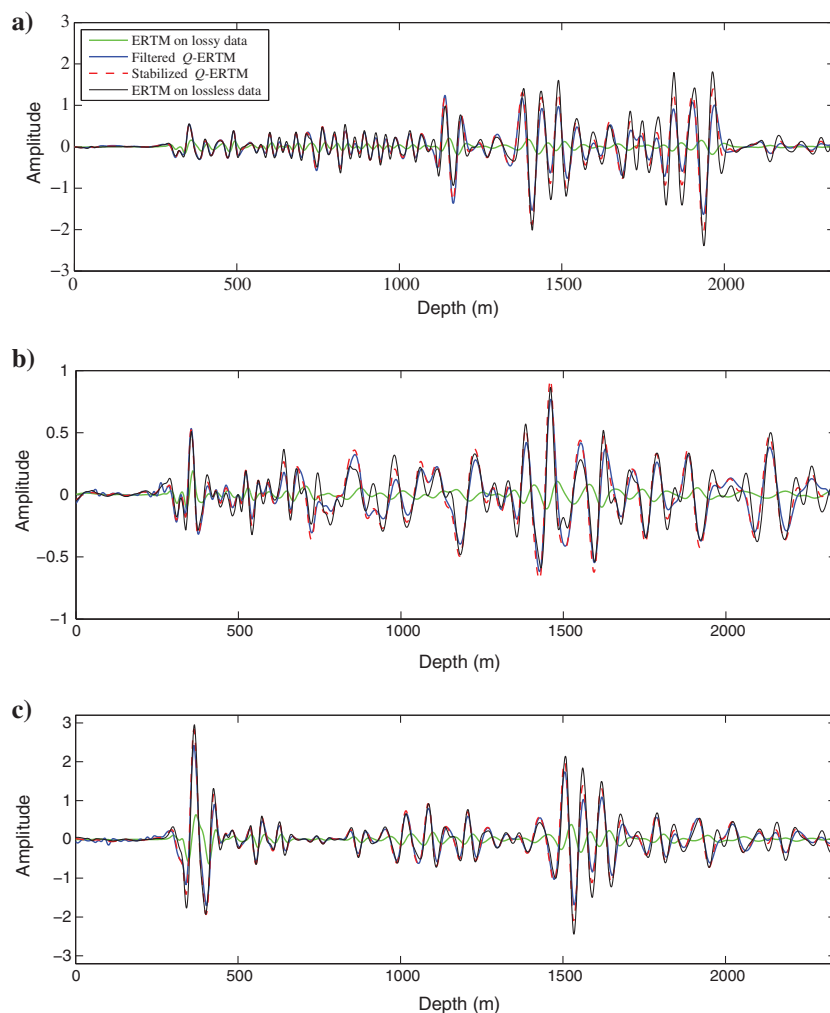


Figure 7. Migrated PP-traces selected arbitrarily from PP-imaging results at three distances of (a) 1.6 km, (b) 3.8 km, and (c) 5.2 km. In each figure, the black line stands for the reference trace, the blue line for the conventional filtered one, the red line for the adaptively stabilized one, and the green line for the noncompensated one.

Figure 8. Migrated PS-traces selected arbitrarily from PS-imaging results at three distances of (a) 1.6 km, (b) 3.8 km, and (c) 5.2 km. In each figure, the black line stands for the reference trace, the blue line for the conventional filtered one, the red line for the adaptively stabilized one, and the green line for the noncompensated one.

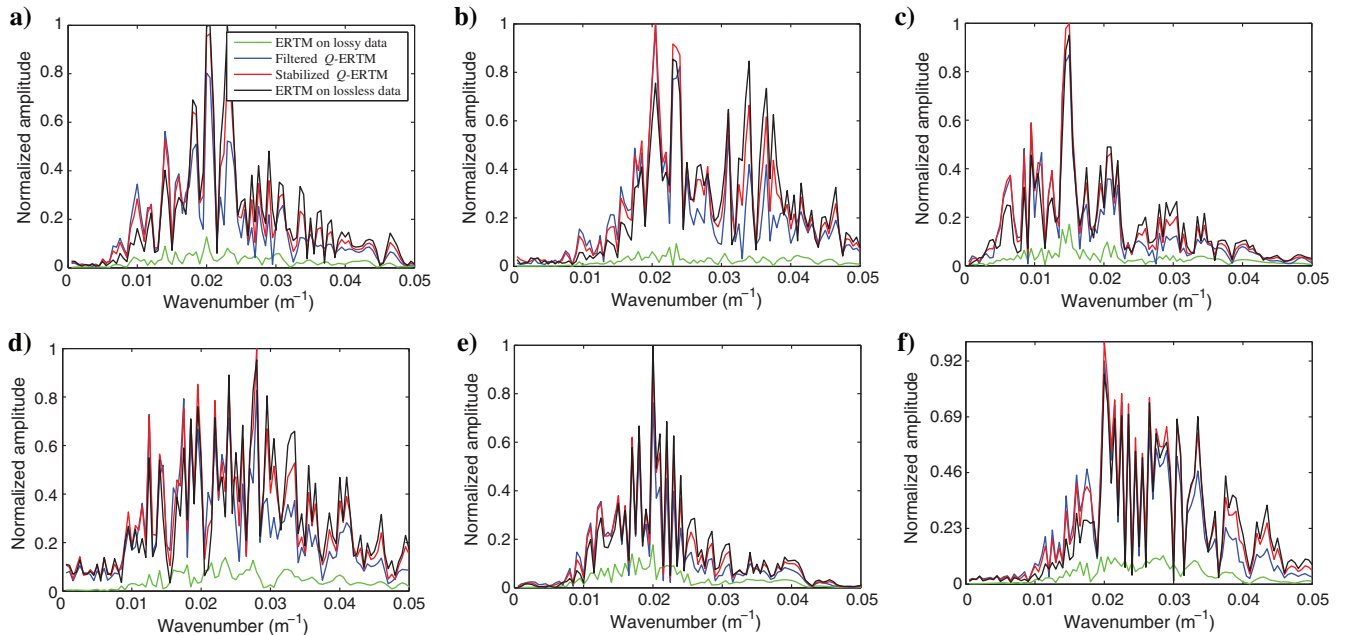
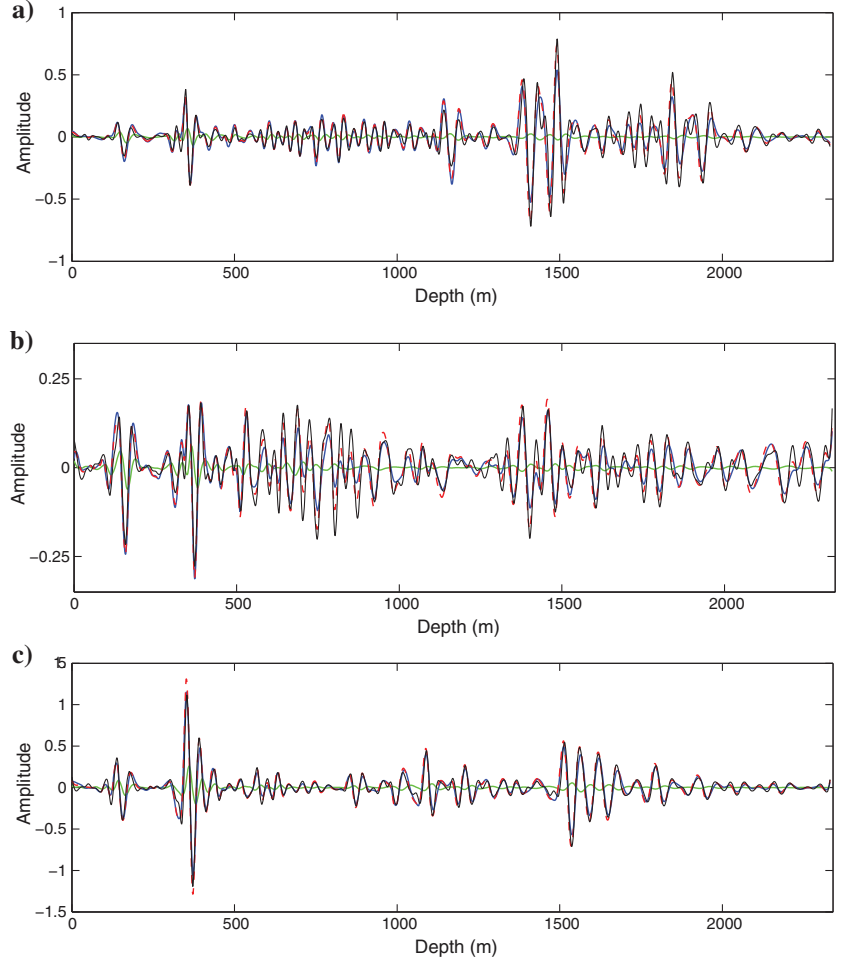


Figure 9. Wavenumber spectra corresponding to the traces shown in Figures 7 and 8, in which the black lines stand for the spectra of the reference traces, the blue lines for the conventional filtered ones, the red lines for the adaptively stabilized ones, and the green lines for the noncompensated ones.

ure 6c and 6d below the unconformities. Figure 6e and 6f shows compensated images by  $Q$ -ERTM using the conventional low-pass filtering method. Figure 6g and 6h depicts the imaging results obtained by our proposed adaptive stabilization scheme. From these migration images, we can find that the compensated results definitely improve the imaging quality and obviously exhibit clear anticlinal structure and recovered amplitudes compared with the noncompensated images. Furthermore, the PS-images enjoy better resolution than that of the PP-images to some degree. For a clearer comparison, Figures 7 and 8 show migrated PP- and PS-traces that are selected arbitrarily at three distances of 1.6, 3.0, and 5.2 km from the imaging results shown in Figure 6. From these traces, we find that the compensated traces match well with the reference traces. Meanwhile, the proposed stabilization scheme exhibits a slight fidelity improvement over the low-pass filtering method. It indicates that our developed stabilized  $Q$ -ERTM is capable of improving the imaging quality and relieving it from cumbersome numerical instability. More specifically, we note that the compensated PP-images obtained by the conventional low-pass filtered  $Q$ -ERTM and the proposed stabilized  $Q$ -ERTM exhibit similar compensation performance, whereas the quality of the compensated PS-images differs markedly for these two imaging methods. This difference just shows the validity of the mode-dependent stabilization, which treats the P- and S-wave compensation as two individual procedures and possesses high-frequency noise suppression in conformity with the PP- and PS-imaging processes. Figure 9 shows the wavenumber spectra corresponding to the traces in Figures 7 and 8. We can see that the overall frequency bands of the compensated ones are expanded to a wider range, associated with increased dominant frequency, and they almost reach the same level as the references. This demonstrates that the proposed stabilized  $Q$ -ERTM improves the migration quality in terms of the imaging fidelity and visual resolution.

We initially expect to see great improvement between the proposed method and conventional low-pass filtering; however, the synthetic numerical results fail to fully match the theoretical results shown in Figure 1. A possible explanation is that the improvement in compensation frequency bands may not visibly reflect the resolution improvement on the migrated images. Anyway, the proposed stabilized  $Q$ -ERTM provides a feasible way to stabilize the compensation process with comparable (sometimes better) results. Furthermore, the proposed mode-dependent stabilization scheme can adapt well to the viscoelastic case in which  $Q_p$  and  $Q_s$  can be treated separately. Another possible reason is that the synthetic example without any noise may result in a quite comparable stabilization performance regardless of how broad the compensation frequency bands it preserves. We also provide a field data example in our next subsection to further verify the feasibility of the proposed method.

### $Q$ -ERTM for the field data

The  $Q$ -ERTM for a field data presented here aims to further verify the feasibility of the proposed stabilized  $Q$ -ERTM. We apply the proposed  $Q$ -ERTM to vertical-component-only land seismic data. The surface is flat, and the model

size is  $20 \times 6$  km with a grid interval of 20 m. There are 250 explosive shots horizontally located at an approximate 20 m depth, most of which have an interval of 40 m. The receivers are located at the surface with a 20 m interval, and the maximum offset is 4.8 km. We consider  $nt = 4000$  time steps for each shot with the temporal interval of  $dt = 0.001$  s. To eliminate the diffraction artifacts from long offsets, we set the stacking aperture of 4.0 km around the shot. Figure 10 shows the P- and S-wave velocity models. Because the parameter  $Q_{p,s}$  is usually not available for field data, it can be determined from the following empirical relation (Li, 1993):

$$Q_{p,s} = 3.516v_{p,s}^{2.2}, \quad (31)$$

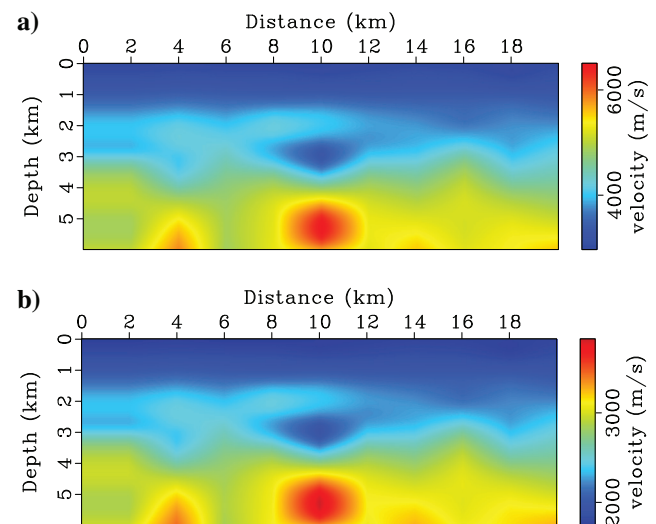


Figure 10. (a) The P-wave velocity and (b) S-wave velocity of the field data.

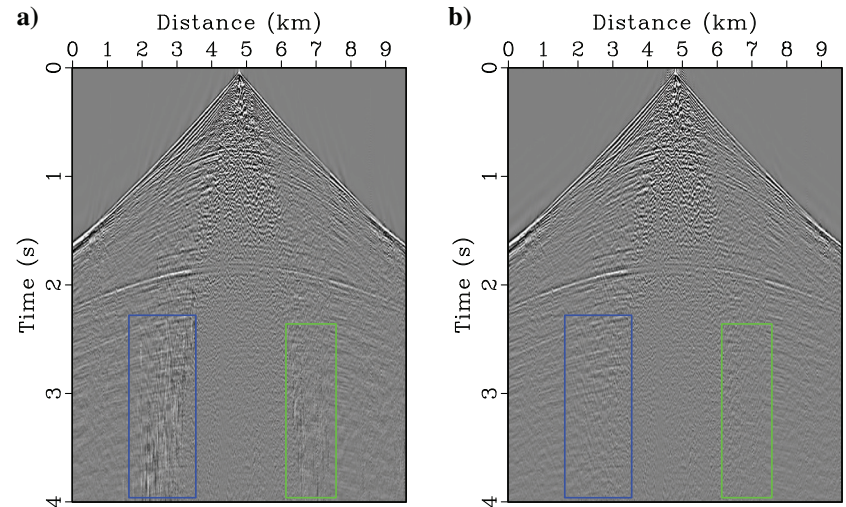


Figure 11. (a) Original and (b) denoised seismogram of the 150th source located at a distance of approximately 11.8 km. We can find that the low-frequency noise shown in the blue and green frames is removed after band-pass filtering.

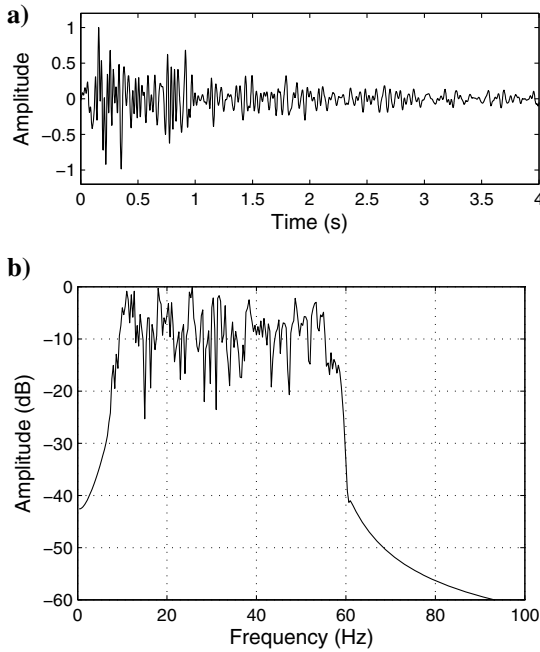


Figure 12. (a) The averaged trace from Figure 11b and (b) its amplitude spectrum in decibel. From this decibel spectrum, we can determine the cutoff frequency  $f_c = 60$  Hz of the low-pass-filtering method.

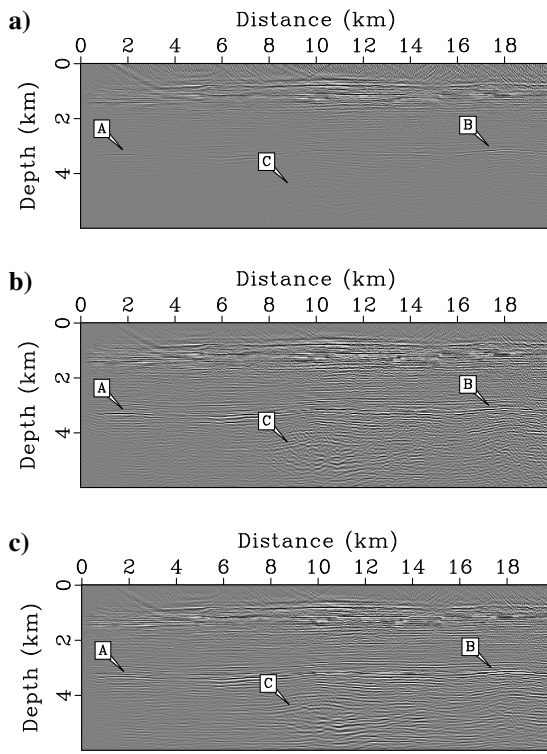


Figure 13. Migrated PP-images obtained from (a) conventional ERTM without attenuation compensation, (b) low-pass-filtered  $Q$ -ERTM, and (c) adaptively stabilized  $Q$ -ERTM, in which labels A and B denote the reflector located at a depth of approximately 3.2 km and label C corresponds to the reflector located at a depth of approximately 4.8 km.

where the P- and S-wave velocity are given in kilometers per second.

Figure 11a shows the observed seismogram of the 150th source located at a distance of approximately 11.8 km, which contains three main reflectors located at depths of approximately 0.8, 1.4, and 2.8 km, respectively. Denoise processes are conducted before performing  $Q$ -ERTM, and the denoised seismogram is shown in Figure 11b. The averaged trace from Figure 11b and its amplitude spectrum are displayed in Figure 12. This spectrum indicates that the dominant frequency of the seismic data is approximately 20 Hz, and the effective frequency band ranges from 8 to 60 Hz. This decibel spectrum provides a prior reference to determine a reasonable cutoff frequency  $f_c$  of the low-pass filtering method and stabilization factor  $\sigma^2$  of the proposed method. Here, we select  $f_c = 60$  Hz and  $\sigma^2 = 2.5 \times 10^{-4}$ .

Figure 13 shows the migrated PP-images using conventional ERTM without attenuation compensation, low-pass filtered  $Q$ -ERTM, and adaptively stabilized  $Q$ -ERTM from field data, respectively. Figure 14 shows the migrated PS-images obtained from these three imaging methods. From Figures 13 and 14, we can find that the compensated images exhibit better stratigraphic continuity, sharper reflectors, and a more balanced amplitude compared to the noncompensated ones. Furthermore, the migrated images using the proposed stabilized-compensation scheme have a higher visual resolution and better structural fidelity compared to the conventional filtered ones. For a clearer comparison, Figure 15 displays the wavenumber spectra of the reference traces selected from the

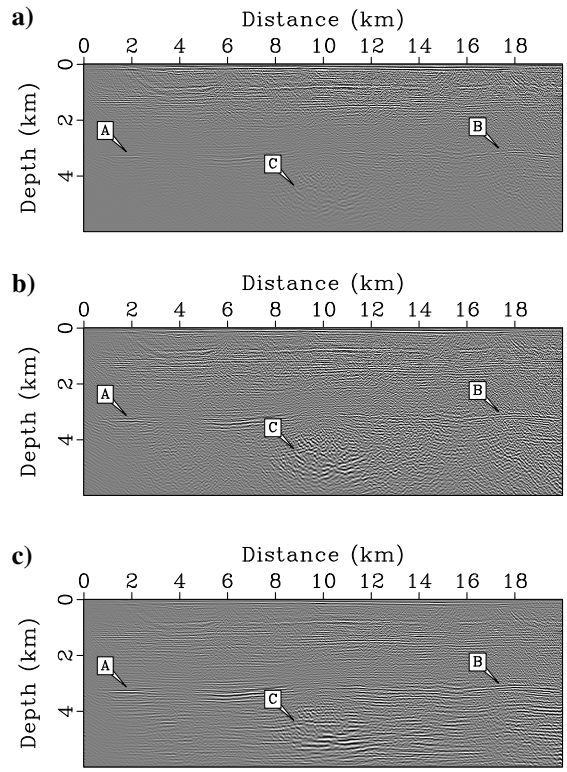


Figure 14. Migrated PS-images obtained from (a) conventional ERTM without attenuation compensation, (b) low-pass-filtered  $Q$ -ERTM, and (c) adaptively stabilized  $Q$ -ERTM, in which labels A and B denote the reflector located at a depth of approximately 3.2 km and label C corresponds to the reflector located at a depth of approximately 4.8 km.

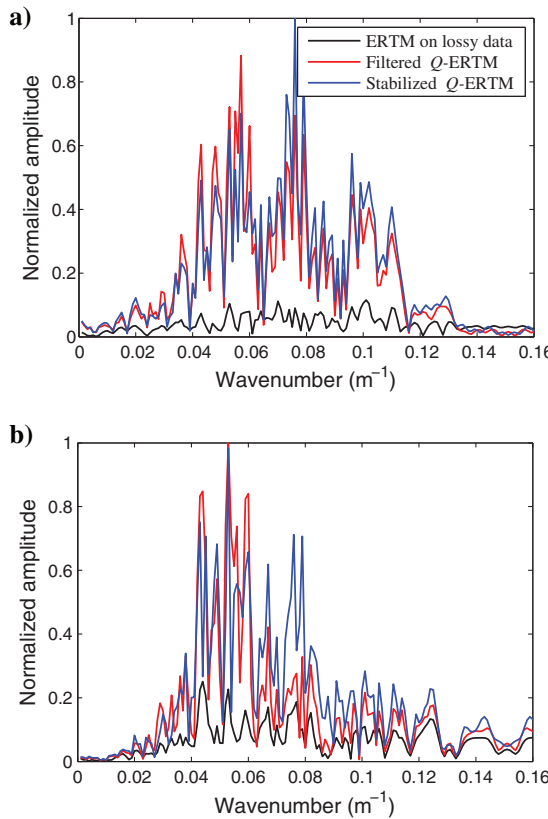


Figure 15. Wavenumber spectra of the reference traces selected from the migrated images ( $X = 6$  km), in which the black lines stand for the spectra of the noncompensated traces, the red lines for the conventional filtered ones, and the blue lines for the adaptively stabilized ones.

migrated PP- and PS-images ( $X = 6$  km). The comparison indicates that the proposed stabilized  $Q$ -ERTM tends to preserve more high-frequency components compared to the conventional filtered  $Q$ -ERTM. Frankly speaking, the field data experiment is definitely more challenging due to the presence of the crosstalk effect and the absence of multicomponent recorded data available. We also admit that our current research mainly focuses on theoretical analysis and synthetic tests, which is far from a sophisticated method for field-data application. In this sense, we would like to step further in our future work and try our best to improve the feasibility of the proposed method.

## CONCLUSION

We have developed a stable  $Q$ -ERTM framework for multi-component seismic imaging, in which the mode-dependent adaptive stabilization operator is an extension of the previously formulated version for  $Q$ -ARTM. The SGPS approach and vector-based P- and S-wavefield decomposition scheme are also introduced to realize an efficient wavefield extrapolation and viable imaging condition for  $Q$ -ERTM. We have provided the synthetic and field data experiments to verify the superiority of the proposed approach in terms of fidelity and stability. The theoretical analysis and numerical results indicate that the proposed scheme has the ability to handle the issue of numerical instability arising from the viscoelastic compen-

sation and exhibits superior properties of time variance and  $Q$  dependence over a commonly used low-pass filtering method.

## ACKNOWLEDGMENTS

We thank H. Chen and N. Wang for inspiring discussions about modeling for viscoelastic wave equation with DFLs. We are grateful to the developers of the Madagascar software package for providing codes for testing the algorithms and preparing the figures. This work was financially supported in part by the National Natural Science Foundation of China (grant no. 41630314), the National Science and Technology Program (grant no. 2016ZX05010001), Major Project of the China National Petroleum Corporation (grant no. 2016A-3302), and Scientific Research and Development of CNPC (grant no. 2017D-5006-16). Y. Wang is financially supported by the China Scholarship Council.

## DATA AND MATERIALS AVAILABILITY

Data associated with this research are available and can be obtained by contacting the corresponding author.

## APPENDIX A VISCOELASTIC P- AND S-WAVEFIELDS DECOMPOSITION

In this appendix, we present the vector-based P- and S-wavefields decomposition method of the viscoelastic wave equation with DFLs, following the works of Xiao and Leaney (2010) and Wang et al. (2015). Wang et al. (2015) explicitly derive the decomposed wave equations and point out that the decomposition can be accomplished during wavefield propagation process. This way, the amplitude and phase information are accurately preserved. Xiao and Leaney (2010) give the P- and S-wave components in an elastic isotropic homogeneous medium

$$\begin{cases} \rho \frac{\partial^2 \mathbf{u}_p}{\partial t^2} = (\lambda + 2\mu) \nabla (\nabla \cdot \mathbf{u}), \\ \rho \frac{\partial^2 \mathbf{u}_s}{\partial t^2} = -\mu \nabla \times (\nabla \times \mathbf{u}), \end{cases} \quad (\text{A-1})$$

and defined an intermediate variable  $\sigma_p$  that satisfies

$$\frac{\partial \sigma_p}{\partial t} = (\lambda + 2\mu) \left( \frac{\partial v_x}{\partial x} + \frac{\partial v_z}{\partial z} \right). \quad (\text{A-2})$$

For the viscoelastic case, we replace the Lamé coefficients in equation A-1 with the generalized Lamé coefficients. Taking  $x$ -component, for instance, we have

$$\begin{aligned} \rho \frac{\partial^2 u_{xp}}{\partial t^2} &= (\bar{\lambda} + 2\bar{\mu}) \frac{\partial}{\partial x} \left( \frac{\partial u_x}{\partial x} + \frac{\partial u_z}{\partial z} \right) \\ &= (\eta_p \mathbf{D}_p + \tau_p \mathbf{A}_p \partial_t) \frac{\partial}{\partial x} \left( \frac{\partial u_x}{\partial x} + \frac{\partial u_z}{\partial z} \right), \end{aligned} \quad (\text{A-3})$$

and as  $v_x = \partial u_x / \partial t$ , equation A-3 becomes

$$\rho \frac{\partial^2 v_{xp}}{\partial t^2} = (\eta_p \mathbf{D}_p + \tau_p \mathbf{A}_p \partial_t) \times \frac{\partial}{\partial x} \left( \frac{\partial v_x}{\partial x} + \frac{\partial v_z}{\partial z} \right). \quad (\text{A-4})$$

In a similar way, an intermediate variable  $\sigma_p$  can be obtained by replacing the Lamé coefficients in equation A-2 with the generalized Lamé coefficients, which satisfies

$$\begin{aligned} \frac{\partial \sigma_p}{\partial t} &= (\bar{\lambda} + 2\bar{\mu}) \left( \frac{\partial v_x}{\partial x} + \frac{\partial v_z}{\partial z} \right) \\ &= (\eta_p \mathbf{D}_p + \tau_p \mathbf{A}_p \partial_t) \left( \frac{\partial v_x}{\partial x} + \frac{\partial v_z}{\partial z} \right). \end{aligned} \quad (\text{A-5})$$

Thus, we can get the decoupled wavefield

$$\rho \frac{\partial v_{xp}}{\partial t} = \frac{\partial \sigma_p}{\partial x}. \quad (\text{A-6})$$

We obtain the  $z$ -component in a similar way, which is given by

$$\rho \frac{\partial v_{zp}}{\partial t} = \frac{\partial \sigma_p}{\partial z}. \quad (\text{A-7})$$

If we define an intermediate variable  $\sigma_s$ , we can do similar deduction for the S-component, and then we have

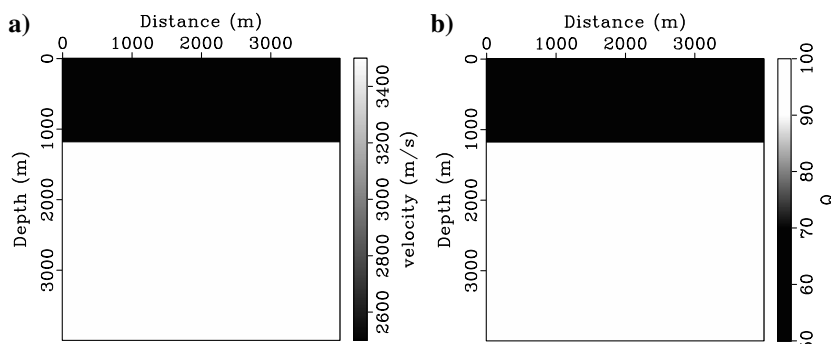


Figure A-1. (a) The P-wave velocity and (b)  $Q_p$  of the two-layer model. The S-wave velocity  $c_s$  and S-wave quality factor  $Q_s$  are obtained by setting  $c_p/c_s = 1.7$  and  $Q_p/Q_s = 1.3$ .

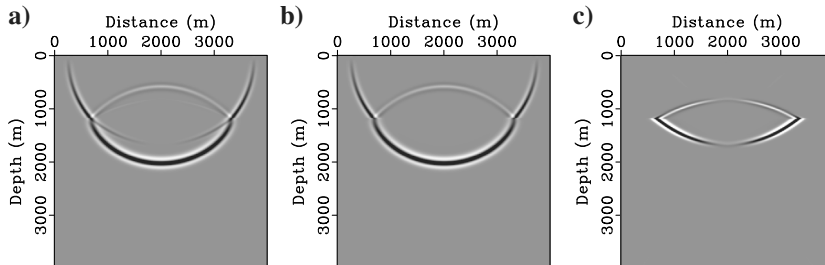


Figure A-2. The  $z$ -component of the (a) coupled viscoelastic wave snapshot, (b) de-coupled P-wave snapshot, and (c) de-coupled S-wave snapshot.

$$\begin{aligned} \frac{\partial \sigma_s}{\partial t} &= -\bar{\mu} \left( \frac{\partial v_z}{\partial x} - \frac{\partial v_x}{\partial z} \right) \\ &= -(\eta_s \mathbf{D}_s + \tau_s \mathbf{A}_s \partial_t) \left( \frac{\partial v_z}{\partial x} - \frac{\partial v_x}{\partial z} \right), \end{aligned} \quad (\text{A-8})$$

and the particle-velocity components are given by

$$\rho \frac{\partial v_{xs}}{\partial t} = \frac{\partial \sigma_s}{\partial z} \quad (\text{A-9})$$

and

$$\rho \frac{\partial v_{zs}}{\partial t} = -\frac{\partial \sigma_s}{\partial x}. \quad (\text{A-10})$$

Equations A-5–A-10 are the decoupled viscoelastic wave equations. We rewrite these equations in a matrix form to obtain equation 17.

To demonstrate the performance of the viscoelastic P- and S-wave-fields decomposition, we conduct viscoelastic simulation and decomposition on a two-layer model with horizontal sharp interface (Figure A-1). Figure A-2 presents the  $z$ -component of the coupled viscoelastic wave snapshot, decoupled P- and S-wave snapshots. From Figure A-2, we can find that the P-wave and converted S-wave are well-separated by the proposed method with only a slight abnormal energy along the interface, which can be removed by smooth or median filtering (Du et al., 2017). Basically, the decoupled P- and S-wave equations can provide satisfactory separation results for Q-ERTM.

## REFERENCES

- Ammari, H., E. Bretin, J. Garnier, and A. Wahab, 2013, Time reversal algorithms in viscoelastic media: European Journal of Applied Mathematics, **24**, 565–600.
- Bai, M., X. Chen, J. Wu, G. Liu, Y. Chen, H. Chen, and Q. Li, 2016,  $Q$ -compensated migration by Gaussian beam summation method: Journal of Geophysics and Engineering, **13**, 35–48.
- Chen, H., H. Zhou, Q. Zhang, and Y. Chen, 2017, Modeling elastic wave propagation using k-space operator-based temporal high-order staggered-grid finite-difference method: IEEE Transactions on Geoscience and Remote Sensing, **55**, 801–815.
- Clarke, G. K., 1968, Time-varying deconvolution filters: Geophysics, **33**, 936–944, doi: [10.1190/1.1439987](https://doi.org/10.1190/1.1439987).
- Dellinger, J., and J. Etgen, 1990, Wave-field separation in two-dimensional anisotropic media: Geophysics, **55**, 914–919, doi: [10.1190/1.1442906](https://doi.org/10.1190/1.1442906).
- Deng, F., and G. A. McMechan, 2008, Viscoelastic true-amplitude prestack reverse-time depth migration: Geophysics, **73**, no. 4, S143–S155, doi: [10.1190/1.2938083](https://doi.org/10.1190/1.2938083).
- Du, Q., C. F. Guo, Q. Zhao, X. Gong, C. Wang, and X. Y. Li, 2017, Vector-based elastic reverse time migration based on scalar imaging condition: Geophysics, **82**, no. 2, S111–S127, doi: [10.1190/geo2016-0146.1](https://doi.org/10.1190/geo2016-0146.1).
- Du, Q., Y. Zhu, and J. Ba, 2012, Polarity reversal correction for elastic reverse time migration: Geophysics, **77**, no. 2, S31–S41, doi: [10.1190/geo2011-0348.1](https://doi.org/10.1190/geo2011-0348.1).
- Griffiths, L., F. Smolka, and L. Tremblay, 1977, Adaptive deconvolution: A new technique for processing time-varying seismic data: Geophysics, **42**, 742–759, doi: [10.1190/1.1440743](https://doi.org/10.1190/1.1440743).
- Guo, P., and G. A. McMechan, 2015, Separation of absorption and dispersion effects in  $Q$ -compensated viscoelastic RTM: 85th Annual International Meeting,

- SEG, Expanded Abstracts, 3966–3971, doi: [10.1190/segam2015-5824203.1](https://doi.org/10.1190/segam2015-5824203.1).
- Guo, P., G. A. McMechan, and H. Guan, 2016, Comparison of two viscoacoustic propagators for  $Q$ -compensated reverse time migration: *Geophysics*, **81**, no. 5, S281–S297, doi: [10.1190/geo2015-0557.1](https://doi.org/10.1190/geo2015-0557.1).
- Hargreaves, N. D., and A. J. Calvert, 1991, Inverse  $Q$  filtering by Fourier transform: *Geophysics*, **56**, 424–576, doi: [10.1190/1.1443067](https://doi.org/10.1190/1.1443067).
- Huang, C., L. Nie, R. W. Schoonover, L. V. Wang, and M. A. Anastasio, 2012, Photoacoustic computed tomography correcting for heterogeneity and attenuation: *Journal of Biomedical Optics*, **17**, 318–321, doi: [10.1117/1.jbo.17.6.061211](https://doi.org/10.1117/1.jbo.17.6.061211).
- Li, Q., 1993, High resolution seismic data processing: Petroleum Industry Press.
- Margrave, G. F., M. P. Lamoureux, and D. C. Henley, 2011, Gabor deconvolution: Estimating reflectivity by nonstationary deconvolution of seismic data: *Geophysics*, **76**, no. 3, W15–W30, doi: [10.1190/1.3560167](https://doi.org/10.1190/1.3560167).
- Mittet, R., 2007, A simple design procedure for depth extrapolation operators that compensate for absorption and dispersion: *Geophysics*, **72**, no. 2, S105–S112, doi: [10.1190/1.2431637](https://doi.org/10.1190/1.2431637).
- Mittet, R., R. Sollie, and K. Hokstad, 1995, Prestack depth migration with compensation for absorption and dispersion: *Geophysics*, **60**, 1485–1494, doi: [10.1190/1.1443882](https://doi.org/10.1190/1.1443882).
- Sun, J., and T. Zhu, 2015, Stable attenuation compensation in reverse-time migration: 85th Annual International Meeting, SEG, Expanded Abstracts, 3942–3947, doi: [10.1190/segam2015-5888552.1](https://doi.org/10.1190/segam2015-5888552.1).
- Sun, J., T. Zhu, and S. Fomel, 2014, Viscoacoustic modeling and imaging using low-rank approximation: *Geophysics*, **80**, no. 5, A103–A108, doi: [10.1190/geo2015-0083.1](https://doi.org/10.1190/geo2015-0083.1).
- Treeby, B. E., 2013, Acoustic attenuation compensation in photoacoustic tomography using time-variant filtering: *Journal of Biomedical Optics*, **18**, 231–236.
- Treeby, B. E., and B. T. Cox, 2010, Modeling power law absorption and dispersion for acoustic propagation using the fractional Laplacian: *Journal of the Acoustical Society of America*, **127**, 2741–2748.
- Treeby, B. E., E. Z. Zhang, and B. T. Cox, 2010, Photoacoustic tomography in absorbing acoustic media using time reversal: *Inverse Problems*, **26**, 115003–20.
- Wang, N., H. Zhou, H. Chen, M. Xia, S. Wang, J. Fang, and P. Sun, 2018a, A constant fractional-order viscoelastic wave equation and its numerical simulation scheme: *Geophysics*, **83**, no. 1, T39–T48, doi: [10.1190/geo2016-0609.1](https://doi.org/10.1190/geo2016-0609.1).
- Wang, W., G. A. McMechan, and Q. Zhang, 2015, Comparison of two algorithms for isotropic elastic P and S vector decomposition: *Geophysics*, **80**, no. 4, T147–T160, doi: [10.1190/geo2014-0563.1](https://doi.org/10.1190/geo2014-0563.1).
- Wang, Y., 2002, A stable and efficient approach of inverse  $Q$  filtering: *Geophysics*, **67**, 657–663, doi: [10.1190/1.1468627](https://doi.org/10.1190/1.1468627).
- Wang, Y., 2006, Inverse  $Q$ -filter for seismic resolution enhancement: *Geophysics*, **71**, no. 3, V51–V60, doi: [10.1190/1.2192912](https://doi.org/10.1190/1.2192912).
- Wang, Y., X. Ma, H. Zhou, and Y. Chen, 2018b, L1-2 minimization for exact and stable seismic attenuation compensation: *Geophysical Journal International*, **213**, 1629–1646.
- Wang, Y., H. Zhou, H. Chen, and Y. Chen, 2018c, Adaptive stabilization for  $Q$ -compensated reverse time migration: *Geophysics*, **83**, no. 1, S15–S32, doi: [10.1190/geo2017-0244.1](https://doi.org/10.1190/geo2017-0244.1).
- Wang, Y., H. Zhou, Q. Li, X. Zhao, X. Zhao, and Y. An, 2017a, Regularized  $Q$ -RTM using time-variant filtering in the k-space: 79th Annual International Conference and Exhibition, EAGE, Extended Abstracts, doi: [10.3997/2214-4609.201700676](https://doi.org/10.3997/2214-4609.201700676).
- Wang, Y., H. Zhou, Q. Zhang, X. Zhao, Z. Zhou, and Y. An, 2017b, Wavefield reconstruction in attenuating media using time-reversal checkpointing and k-space filtering: 79th Annual International Conference and Exhibition, EAGE, Extended Abstracts, doi: [10.3997/2214-4609.201701152](https://doi.org/10.3997/2214-4609.201701152).
- Wang, Y., H. Zhou, X. Zhao, M. Xia, and X. Cai, 2017c, The k-space Green's functions for decoupled constant- $Q$  wave equation and its adjoint equation: 79th Annual International Conference and Exhibition, EAGE, Extended Abstracts, doi: [10.3997/2214-4609.201701153](https://doi.org/10.3997/2214-4609.201701153).
- Wang, Y., H. Zhou, X. Zhao, Q. Zhang, P. Zhao, X. Yu, and Y. Chen, 2019, CuQ-RTM: A CUDA-based code package for stable and efficient  $Q$ -compensated reverse time migration: *Geophysics*, **84**, no. 1, F1–F15, doi: [10.1190/geo2017-0624.1](https://doi.org/10.1190/geo2017-0624.1).
- Xiao, X., and W. S. Leaney, 2010, Local vertical seismic profiling (VSP) elastic reverse-time migration and migration resolution: Salt-flank imaging with transmitted P-to-S waves: *Geophysics*, **75**, no. 2, S35–S49, doi: [10.1190/1.3309460](https://doi.org/10.1190/1.3309460).
- Yan, J., and P. Sava, 2008, Isotropic angle-domain elastic reverse-time migration: *Geophysics*, **73**, no. 6, S229–S239, doi: [10.1190/1.2981241](https://doi.org/10.1190/1.2981241).
- Yang, P., R. Brossier, L. Métivier, and J. Virieux, 2016, Wavefield reconstruction in attenuating media: A checkpointing-assisted reverse-forward simulation method: *Geophysics*, **81**, no. 6, R349–R362, doi: [10.1190/geo2016-0082.1](https://doi.org/10.1190/geo2016-0082.1).
- Yilmaz, O., and S. M. Doherty, 2001, Seismic data analysis: Processing, inversion, and interpretation of seismic data: SEG.
- Zhang, J., Z. Tian, and C. Wang, 2007, P-and S-wave separated elastic wave equation numerical modeling using 2D staggered-grid: 77th Annual International Meeting, SEG, Expanded Abstracts, 2104–2109, doi: [10.1190/1.2792904](https://doi.org/10.1190/1.2792904).
- Zhang, J., J. Wu, and X. Li, 2012, Compensation for absorption and dispersion in prestack migration: An effective  $Q$  approach: *Geophysics*, **78**, no. 1, S1–S14, doi: [10.1190/geo2012-0128.1](https://doi.org/10.1190/geo2012-0128.1).
- Zhang, X., Q. Du, S. Zhang, and C. Guo, 2017, Vector-based elastic reverse time migration based on proposed energy-normed imaging condition: 87th Annual International Meeting, SEG, Expanded Abstracts, 2466–2470, doi: [10.1190/segam2017-17683169.1](https://doi.org/10.1190/segam2017-17683169.1).
- Zhang, Y., P. Zhang, and H. Zhang, 2010, Compensating for visco-acoustic effects in reverse time migration: 80th Annual International Meeting, SEG, Expanded Abstracts, 3160–3164, doi: [10.1190/1.3513503](https://doi.org/10.1190/1.3513503).
- Zhao, X., H. Zhou, Y. Wang, H. Chen, Z. Zhou, P. Sun, and J. Zhang, 2018, A stable approach for  $Q$ -compensated viscoelastic reverse time migration using excitation amplitude imaging condition: *Geophysics*, **83**, no. 5, S459–S476, doi: [10.1190/geo2018-0222.1](https://doi.org/10.1190/geo2018-0222.1).
- Zhu, T., 2016, Implementation aspects of attenuation compensation in reverse-time migration: *Geophysical Prospecting*, **64**, 657–670, doi: [10.1111/1365-2478.12301](https://doi.org/10.1111/1365-2478.12301).
- Zhu, T., and J. M. Carcione, 2014, Theory and modelling of constant- $Q$  P-and S-waves using fractional spatial derivatives: *Geophysical Journal International*, **196**, 1787–1795, doi: [10.1093/gji/gjt483](https://doi.org/10.1093/gji/gjt483).
- Zhu, T., and J. M. Harris, 2014, Modeling acoustic wave propagation in heterogeneous attenuating media using decoupled fractional Laplacians: *Geophysics*, **79**, no. 3, T105–T116, doi: [10.1190/geo2013-0245.1](https://doi.org/10.1190/geo2013-0245.1).
- Zhu, T., J. M. Harris, and B. Biondi, 2014,  $Q$ -compensated reverse-time migration: *Geophysics*, **79**, no. 3, S77–S87, doi: [10.1190/geo2013-0344.1](https://doi.org/10.1190/geo2013-0344.1).
- Zhu, T., and J. Sun, 2017, Viscoelastic reverse time migration with attenuation compensation: *Geophysics*, **82**, no. 2, S61–S73, doi: [10.1190/geo2016-0239.1](https://doi.org/10.1190/geo2016-0239.1).